Fabrication and characterization of La_2O_3–Fe_2O_3–Bi_2O_3 nanopowders: Effects of La_2O_3 addition on structure, optical, and radiation-absorption properties

Jamila S. Alzahrani [a], Manal Hessien [b], Z.A. Alrowaili [c], Imen Kebaili [d], I.O. Olarinoye [e], Halil Arslan [f], M.S. Al-Buriahi [g,*]

[a] *Department of Physics, College of Science, Princess Nourah Bint Abdulrahman University, P.O. Box 84428, Riyadh, 11671, Saudi Arabia*
[b] *Department of Chemistry, College of Science, King Faisal University, P.O. Box 400, Al-Ahsa, 31982, Saudi Arabia*
[c] *Physics Department, College of Science, Jouf University, P.O.Box:2014, Sakaka, Saudi Arabia*
[d] *Department of Physics, Faculty of Science, King Khalid University, P.O. Box 9004, Abha, Saudi Arabia*
[e] *Department of Physics, School of Physical Sciences, Federal University of Technology, Minna, Nigeria*
[f] *Electrical and Electronics Engineering, Sakarya University of Applied Sciences, Sakarya, Turkey*
[g] *Department of Physics, Sakarya University, Sakarya, Turkey*

ARTICLE INFO

ABSTRACT

In this study, we fabricated and characterized six new nanopowders representing variations of La_2O_3–Fe_2O_3–Bi_2O_3, i.e., $100Bi_2O_3$, $30Fe_2O_3$–$70Bi_2O_3$, $3La_2O_3$–$27Fe_2O_3$–$70Bi_2O_3$, $7La_2O_3$–$23Fe_2O_3$–$70Bi_2O_3$, $10La_2O_3$–$20Fe_2O_3$–$70Bi_2O_3$, and $20La_2O_3$–$10Fe_2O_3$–$70Bi_2O_3$ (represented by 100B, 30F70B, 3L27F70B, 10L20F70B, and 20L10F70B, respectively). These nanopowders were prepared by the microwave-assisted hydrothermal synthesis method. Saponin extract from soapnuts was used as the nanoparticle capping agent. The structural, optical, and gamma radiation characteristics were measured, calculated, and analysed, respectively. The chemical structures of the nanocomposites influenced their optical and radiation shielding characteristics. The optical bandgaps of the 100B, 30F70B, 3L27F70B, 7L23F70B, 10L20F70B, and 20L10F70B nanopowders were 3.16, 3.13, 3.43, 3.45, 3.46, and 3.58 eV, respectively. The ranges of the mass attenuation coefficients of the nanopowders were computed, using XCOM, to be 0.0412–5.1624, 0.0401–4.5406, 0.0401–4.5285, 0.0401–4.5129, 0.0401–0.5015, and 0.0400–4.4156 cm^2/g, respectively, and the ranges of mass energy absorption coefficients were found to be 0.0232–1.7525, 0.0228–1.5484, 0.0228–1.5598, 0.0288–1.5746, 0.0228–1.5853, and 0.0227–1.6192 cm^2/g, respectively, for photon energies in the range of 0.1–10 MeV. The order of the dose rate trend was as follows: 30F70B < L27F70B < 7L23F70B < 10L20F70B < 20L10F70B. Analysis of the photon interaction parameters showed that the synthesized nanopowders could function well as fillers in radiation-shielding matrices.

1. Introduction

Nanoparticles (NP), depending on their geometry, are zero-, one-, two, or three-dimensional (0D, 1D, 2D, and 3D, respectively) and technologically versatile materials with dimension(s) less than 100 nm [1,2]. The exceptional features that NPs exhibit, which are dependent on their size and are different from those of corresponding macro particles or bulk materials, make them an interesting class of materials with a wide range of functionality. The technology for synthesis, characterisation, and application of NPs has grown tremendously in the past few decades. Nanoscience technology has become an indispensable tool in multidisciplinary applications in fields such as medicine, agriculture, materials science, energy harvesting, environmental conservation, electronics, and manufacturing [2,3]. Hence, a large number of materials based on NPs have been produced on a commercial scale in recent times.

As a result of their high surface energy, NPs tend to agglomerate easily. This affects their stability and functionality. Instability can be addressed by coating the surfaces of NPs with an appropriate capping material [4]. The capping agent can also control growth, the growth

---
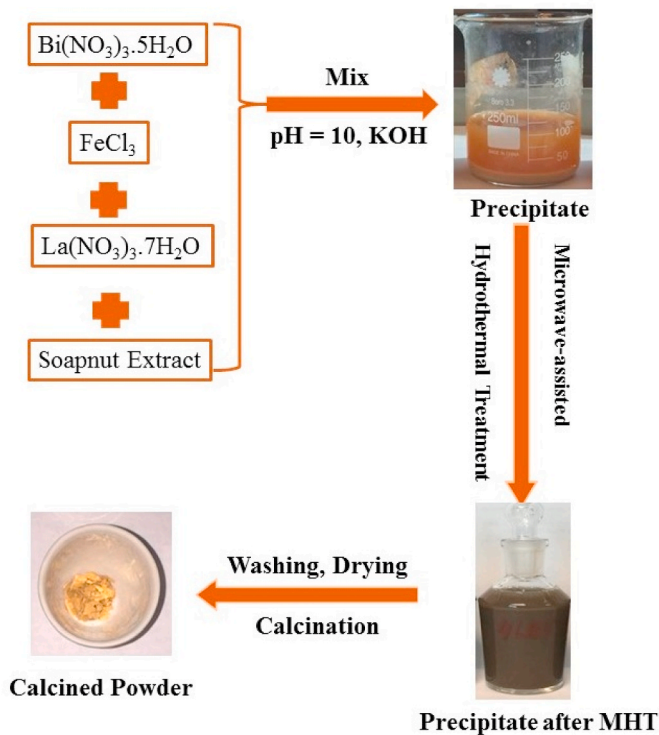
Fig. 1. Synthetic process of $La_2O_3.Fe_2O_3 –Bi_2O_3$ nanocomposites.

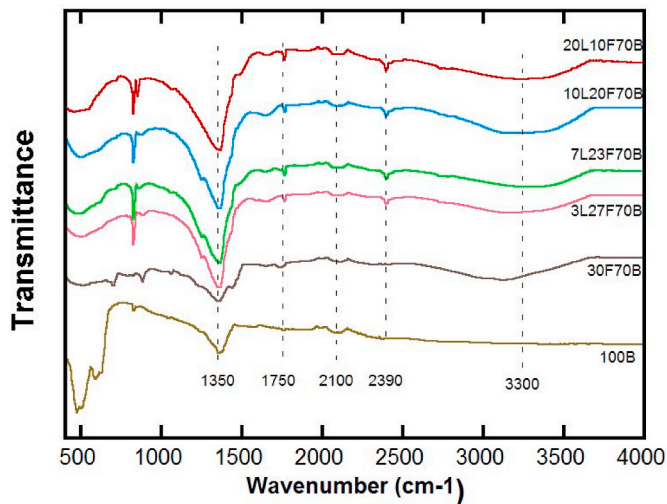**Fig. 2.** Full range-FTIR spectra of the synthesized samples.

Fig. 3. Short range - FTIR spectra of the synthesized samples.

direction, and particle size [5]. A good capping agent should be non-toxic, biodegradable, and compatible with green chemistry. For this reason, biological materials are attractive as capping agents when toxicity and environmental concerns are of major importance. Saponins are natural compounds found in plants and animals which can be used as surfactants and capping agents [6,7]. Their biological sources make them environmentally friendly and non-toxic. One good source of saponins is the soapnut tree (*Sapindus mukurossi*). Soapnut extract has been shown to be a very effective, inexpensive, and biologically safe surfactant and clapping agent [8,9]. These features led to its selection for use in this study.

The use of clapping agents makes NPs stable and attractive in many applications. Metallic, ceramic, polymeric, liquid-based, semiconductor and composite NPs have a wide 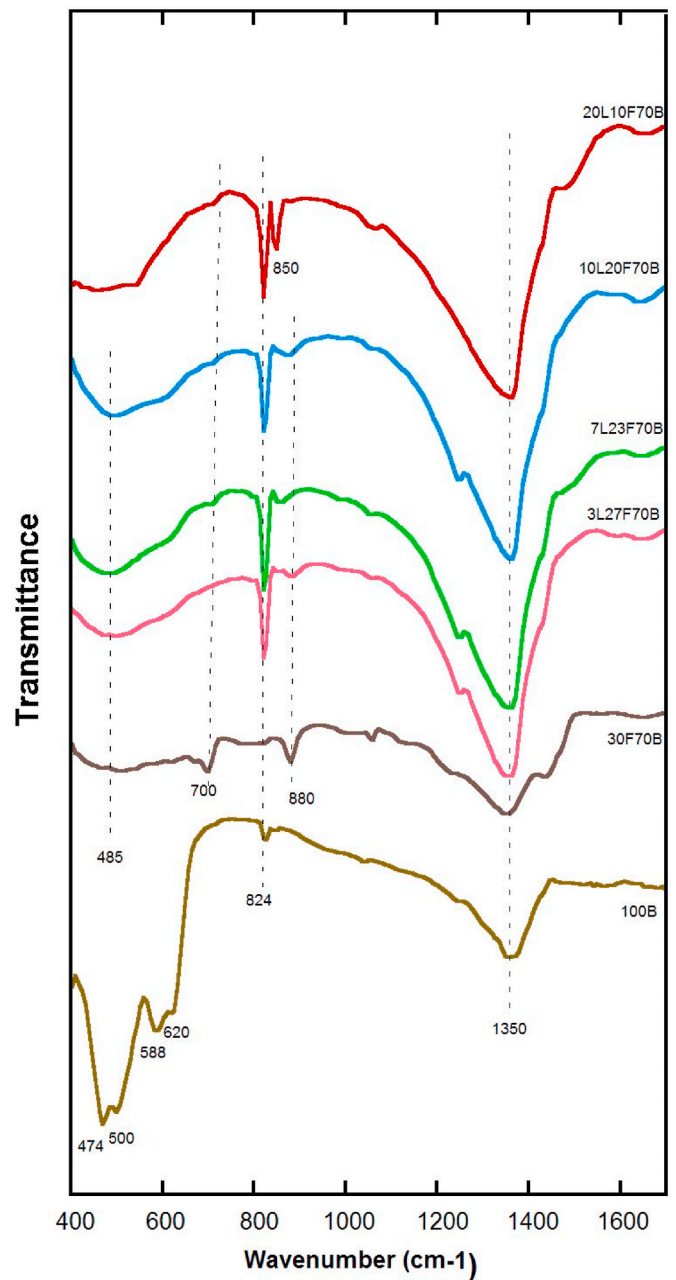spectrum of applications, depending on their properties. The unique attributes NPs offer make them useful in drug and medication development, manufacturing and material development, environmental conservation, purification and pollution control, electronics, renewable energy harvesting and many more applications [1,2].

Some NPs have shown great resistance to ionising radiation (IR), which suggests that they could be used for radiation shielding. Previous studies have shown that multiwall carbon nanotubes (MWCNT) are resistant to IR-induced structural changes, which suggests that they could be effective in charged particle shielding [10–12]. Recently, ZnO and MgO NPs were synthesized by Rashad et al. [13] using the solid state reaction method. Radiation studies of NPs synthesized via FLUKA simulation have shown that ZnO NPs with smaller particle sizes have better radiation-shielding prowess. It has been suggested that ZnO NPs could serve as additives to other materials to enhance their radiation-absorbing capacity. Earlier studies reported that the shielding
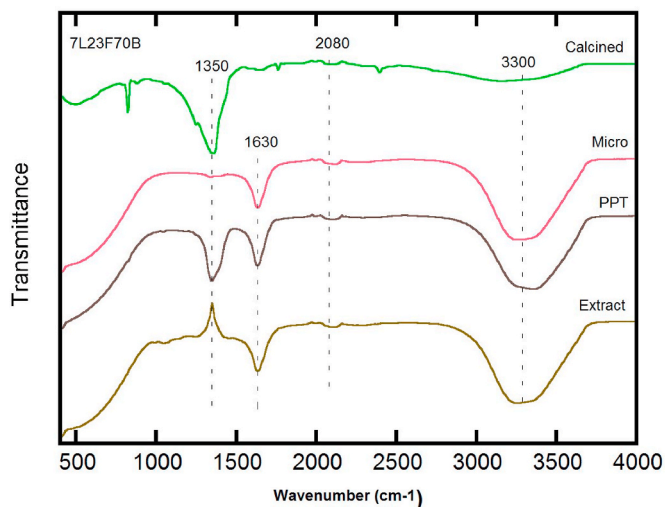
Fig. 4. The FTIR spectra of (a) Saponin extract, of sample 7L23F70B (b) precipitate (c) after hydrothermal-assisted microwave treatment (d) after calcination.
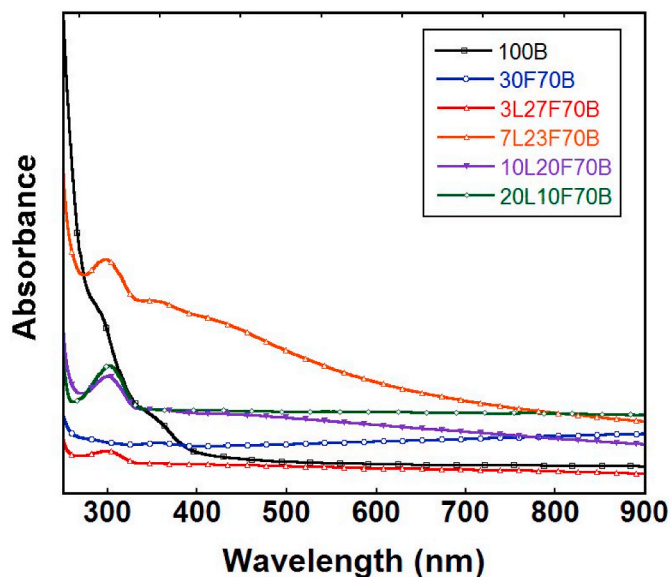

Fig. 5. UV-VIS spectra of the synthesized samples.

capacities of different materials improved when they were infused with NPs [14–16]. The addition of H_4B, Fe_2O_3, WO_3, and PbO_2 NPs and micro particles was discovered to alter the gamma ray and neutron interaction efficiency of ordinary concrete [14], with NPs enhancing the shielding ability of the concrete more than micro particles. The improvement in shielding ability achieved when NPs were infused into concrete was more than 11% than that achieved with micro particles for neutrons in the energy range of 100–3000 keV and at least 19% for photons in the energy range of 142–1250 keV. In another study, Tekin et al. showed that the use of WO_3 NP-doped concrete performed better than concrete doped with WO_3 micro particles [15]. The addition of WO_3, PbO, and Bi_2O_3 NPs has also been confirmed to improve the photon attenuation coefficient of silicon resins [16], with PbO- and Bi_2O_3-impregnated resins exhibiting better attenuation than WO_3-impregnated resin. The same study showed that NPs attenuate photons better than micro particles. The differences in the shielding ability of the WO_3, PbO, and Bi_2O_3 NP-impregnated silicon resin were attributed to differences in the shielding ability of the different fillers (WO_3, PbO, and Bi_2O_3 NPs).

These results indicate that examination of the shielding ability of different types of NPs is important in producing improved or novel shields.

Bi_2O_3, Fe_2O_3, and La_2O_3 are important compounds from a radiation-shielding perspective. Their high densities, i.e., 8.9, 5.24, and 6.51 g/cm^3, respectively, imply that high photon cross sections and high O contents can produce high neutron cross sections. The influence of these compounds and metals (Bi, La, and Fe) on composite materials such as glasses, alloys, and ceramics are well documented [17–23]. In addition, Bi_2O_3 NPs have been found to improve the electron shielding proficiency of poly (methyl-methacrylate)/multi-walled carbon nanotube (PMMA/MWCNT) nanocomposites [24]. Likewise, the photon shielding ability of polymer fabrics has been shown to be enhanced by the addition of Bi_2O_3 NPs [25]. The radiation shielding capacity of ordinary Portland cement paste has been shown to be enhanced by the addition of Fe_2O_3 NPs [26]. The findings of these previous studies suggest that a combination of Bi_2O_3, Fe_2O_3, and La_2O_3 nanocomposites would have outstanding radiation-shielding capacity.

In this paper, we present for the first time the optical, structural, and radiation-shielding parameters of La_2O_3–Fe_2O_3–Bi_2O_3 nanocomposite powders. The influence of the ratio of La_2O_3 to Fe_2O_3 on the properties of the nanocomposites is also reported. The results of this study will be useful in the design of novel radiation shields containing Bi_2O_3–Fe_2O_3–La_2O_3 nanocomposites.

2. Experimentation

2.1. Materials

Analytic-grade bismuth nitrate pentahydrate ($Bi(NO_3)_3·5H_2O$), iron chloride anhydrous ($FeCl_3$), lanthanum nitrate heptahydrate (La$(NO_3)_3·7H_2O$), and potassium hydroxide (KOH) have been purchased from Sigma-Aldrich. Double-distilled water was used to make all of the solutions. Soapnuts were acquired from NatureOli Beautiful in Arizona, USA. These have been sun-dried, de-seeded soap berries that were certified as organic by the US Department of Agriculture (USDA).

2.2. Saponin extraction

The soapnuts have been finely ground using a home grinder, and 1 g of soapnut powder was mixed with 10 ml of deionized water. At a temperature of 60 °C, this mixture was sonicated for 1 hf. Whatman filter paper was used to separate the extract, which was then kept at 4 °C in the refrigerator. This filtrate is referred to hereinafter as saponin extract.

2.3. Microwave-assisted hydrothermal synthesis

The requisite mole percent composition was determined by weighing specific quantities of bismuth nitrate pentahydrate ($Bi(NO_3)_3·5H_2O$), iron chloride anhydrous ($FeCl_3$), and lanthanum nitrate heptahydrate (La($NO_3)_3·7H_2O$). The pH (10), volume of extract (20 mL extract/100 mL salt solution), microwave treatment period (30 min), and temperature (200 °C) were all held constant to avoid affecting the synthesis. The requisite weights were combined with 50 mL of deionized water and 25 mL of saponin extract. The pH of the mixture was adjusted using a 5 M KOH solution. Using a burette, 1 mL of KOH solution was added drop-wise at a rate of 1 mL/min while the mixture was stirred continuously. A Thermo Scientific™ Orion™ 2-Star Benchtop pH meter was used to monitor the pH of the solution until it reached the desired pH of 12 [27]. Fig. 1 illustrates the synthesis procedure. The hydroxide precipitate created previously was transferred to a Teflon jar and heated in a microwave for 30 min at 200 °C. After the liquor was poured, the sample was removed from the microwave and placed in a beaker. The material was then sonicated for 90 min in 50 mL of distilled water using a POWERSONIC 405 system. The solid oxide was then allowed to settle for
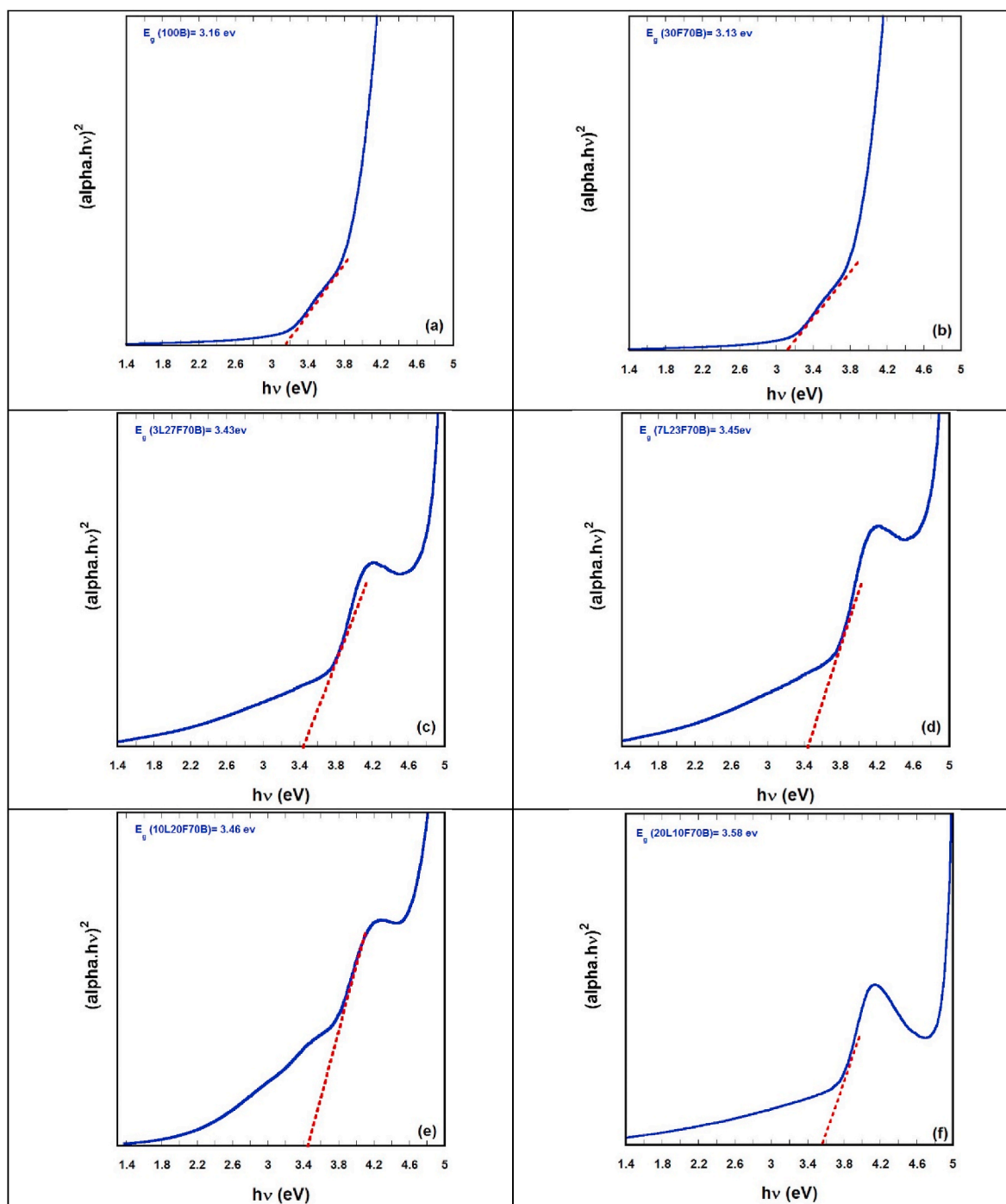
Fig. 6. The Tauc's plots of the synthesized samples.

12 h under gravity, and the liquid was drained out and refilled with 20 mL of ethanol. After a second round of sonication and precipitation, the sample was dried in a 60 °C oven for 12 h. Finally, the samples were calcined for 2 h at 300 °C to remove any organic residue.

2.4. Powder characterization

The Fourier transform infrared (FTIR) spectra of metal oxide nanoparticles and nanocomposites samples were collected using a Cary 630 FTIR spectrophotometer. A UV-1800 spectrophotometer was used to obtain the UV spectra of the nanocomposites (Shimadzu, Kyoto, Japan).

2.5. Gamma ray absorption characterisation

To assess the gamma ray photon-absorbing efficiency of the prepared nanocomposites, the photon attenuation parameters of the La_2O_3–Fe_2O_3–Bi_2O_3 nanocomposite powders, such as the mass attenuation coefficient μ/ρ, mass energy absorption coefficient μ_{en}/ρ, effective atomic number Z_{eff}, effective electron density N_{eff}, specific gamma ray constant Γ, and gamma dose rate were evaluated for photon energies in the range 0.10–10 MeV. The μ/ρ and μ_{en}/ρ of the NP powders was estimated using the well-known free online XCOM computational tool (https://physics.nist.gov/PhysRefData/Xcom/html/xcom1.html). XCOM can calculate the μ/ρ and μ_{en}/ρ values of elements, compounds,
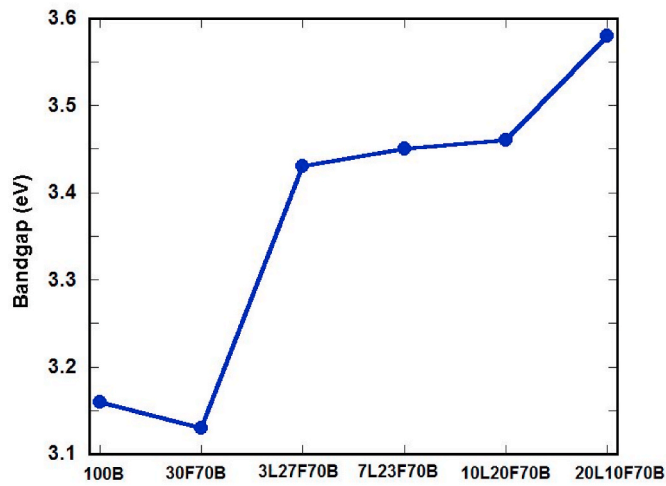
Fig. 7. The bandgap of samples synthesized by a Hydrothermal assisted-Microwave technique and calcined at 300 °C for 2 h as calculated from Tauc's plots.

and mixtures. The addition rule shown as equation (1) was adopted for the mixture and compound calculations [28–33].

$$(\mu/\rho)_{i,\,c} = \sum w_i (\mu/\rho)_{i,\,e} \tag{1}$$

In this equation, $(\mu/\rho)_{i,\,c}$ represents μ/ρ (or μ_{en}/ρ) for compound or mixture c, w_i represents the weight fraction of chemical element e in the compound or mixture, and $(\mu/\rho)_{i,\,e}$ represents μ/ρ (or μ_{en}/ρ) of chemical element e in the compound or mixture. Finally, the i is going on for each element in the compound or for each compound in the mixture. The

values of other radiation absorption parameters for the prepared nano-powders were estimated from these two coefficients, using the following equations [34–37]:

$$Z_{eff} = \frac{\sum_e f_e A_e (\mu/\rho)_e}{\sum_e f_e \frac{A_e}{Z_e} (\mu/\rho)_e} \tag{2}$$

$$N_{eff} = \frac{Z_{eff}}{A} \tag{3}$$

$$\Gamma = \frac{\dot{\Psi}(\mu_{en}/\rho)_c}{4\pi r^2} \tag{4}$$

$$\dot{D} = \frac{A\Gamma}{d^2} \tag{5}$$

In these equations, $\dot{\Psi}$, A, d, and A represent the energy fluence rate, the activity of a single energy photon source, and the mean molar mass and thickness, respectively, of an absorbing medium.

3. Results and discussion

3.1. FTIR characterization

Fig. 2 presents the FTIR spectra for 100B, 3L27F70B, 7L23F70B, 10L20F70B, 15L15F70B, and 20L10F70B after calcination. Peaks in the range of 3000 to 3600 cm^{-1} suggest OH group stretching vibrations, whereas peaks around 1600 cm^{-1} indicate OH group bending vibrations. These peaks are very shallow because of calcination. The small peaks at 2390 cm^{-1} represent the absorbed CO_2 from the surroundings, and those at 1750 cm^{-1} represent stretching of CO. Peaks around 2100 cm^{-1} have been reported in literature for Si–H, which in this case may be referred to as Bi–H and hydrogen being absorbed from the surroundings.

Table 1
Sample code and weight fraction (wt.%) of the prepared nanopowders.

Sample code	Composition (mol %)	Chemical composition (wt.%)			
		O	Fe	La	Bi
100B	100Bi$_2$O$_3$	10.30095	0.00000	0.00000	89.69905
30F70B	30Fe$_2$O$_3$–70Bi$_2$O$_3$	12.83104	8.95752	0.00000	78.21144
3L27F70B	3La$_2$O$_3$–27Fe$_2$O$_3$–70Bi$_2$O$_3$	12.66235	7.95578	2.19873	77.18315
7L23F70B	7La$_2$O$_3$–23Fe$_2$O$_3$–70Bi$_2$O$_3$	12.44421	6.66038	5.04198	75.85342
10L20F70B	10La$_2$O$_3$–20Fe$_2$O$_3$–70Bi$_2$O$_3$	12.28548	5.71776	7.11095	74.88581
20L10F70B	20La$_2$O$_3$–10Fe$_2$O$_3$–70Bi$_2$O$_3$	11.78443	2.74227	13.64183	71.83147

Table 2
Mass attenuation coefficient of the prepared nanopowders via XCOM at different photon energies.

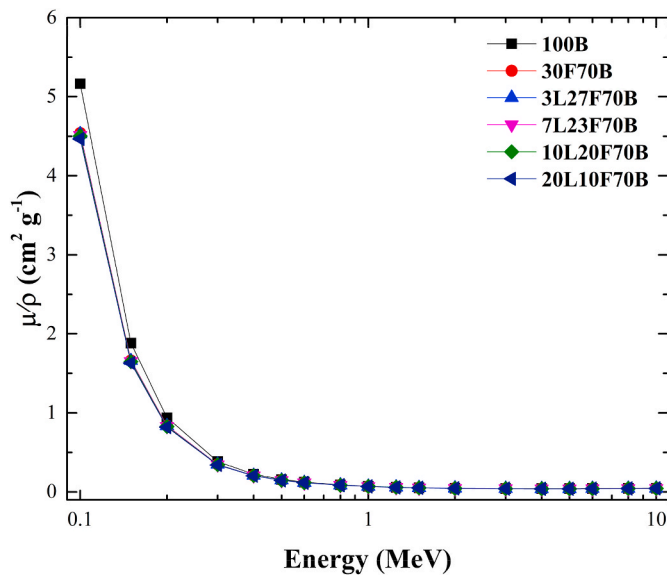| Energy (MeV)	μ/ρ (cm^2/g)					
	100B	30F70B	3L27F70B	7L23F70B	10L20F70B	20L10F70B
0.1	5.16244	4.54057	4.52849	4.51287	4.50151	4.46564
0.15	1.88190	1.66372	1.65823	1.65112	1.64596	1.62964
0.2	0.93961	0.83712	0.83414	0.83029	0.82749	0.81865
0.3	0.38455	0.34926	0.34801	0.34639	0.34522	0.34150
0.4	0.22435	0.20772	0.20702	0.20612	0.20546	0.20338
0.5	0.15751	0.14823	0.14777	0.14718	0.14674	0.14537
0.6	0.12283	0.11711	0.11677	0.11634	0.11602	0.11502
0.8	0.08836	0.08577	0.08556	0.08528	0.08507	0.08444
1	0.07127	0.06997	0.06981	0.06960	0.06946	0.06899
1.25	0.05927	0.05867	0.05855	0.05839	0.05828	0.05792
1.5	0.05275	0.05236	0.05226	0.05213	0.05204	0.05174
2	0.04638	0.04598	0.04590	0.04581	0.04574	0.04551
3	0.04209	0.04133	0.04129	0.04123	0.04119	0.04107
4	0.04124	0.04012	0.04010	0.04008	0.04006	0.04000
5	0.04159	0.04015	0.04015	0.04015	0.04015	0.04015
6	0.04243	0.04072	0.04073	0.04075	0.04076	0.04080
8	0.04472	0.04254	0.04258	0.04262	0.04266	0.04276
10	0.04723	0.04467	0.04472	0.04479	0.04484	0.04499

Fig. 8. Variation of mass attenuation coefficient with respect to a function of photon energy in the prepared nanopowders.

Fig. 3 illustrates the FTIR short range, highlighting where the peaks in this range are located. Sample 100B, which is composed of 100 mol.% Bi_2O_3, shows a broad band between 400 and 640 cm^{-1}, with strong peaks around 474, 500, 588, and 620 cm^{-1}, which are characteristic of Bi–O, and a strong broad peak centred around 1350 cm^{-1}, which is characteristic of Bi–O–Bi. For sample 30F70B, which is composed of 30 mol.% Fe_2O_3.70 mol.% Bi_2O_3. The peaks round 485 and 1350 cm^{-1} are characteristics of Bi–O and Bi–O–Bi, respectively. In addition, two new peaks are visible around 700 and 880 cm^{-1}, which may be due to iron oxide. It has been reported that iron oxide exhibits a strong peak around 570 cm^{-1}, which may overlap the broad peak of bismuth oxide. For the other spectra, a strong sharp peak characteristic of La_2O_3 is centred around 824 cm^{-1} [38]. The FTIR results confirm the successful formation of La_2O_3–Fe_2O_3–Bi_2O_3 nanocomposites [27,39,40].

To further understand the influence of the synthesis procedures on the saponin extract, Fig. 4 was produced to show the FTIR spectra (a) of the saponin extract for sample 7L23F70B, (b) of the precipitate, (c) after the production treatment, and (d) after calcination. Fig. 4(a) shows peaks of 2150–2010 cm^{-1} indicating CH_2 stretching, peaks in the range

of 3700–2800 cm^{-1} indicating hydroxyl (OH) group stretching, peaks in the range of 1740–1530 cm^{-1} indicating carbonyl (C=O) groups and C=C alkenes, and peaks in the range of 1110–950 cm^{-1} indicating C–O–C [5,6]. The existence of saponin in the aqueous soapnut solution is confirmed by the concordance of the peaks observed for the saponin aqueous extract with those reported in the literature [41–47]. Fig. 4(b) shows 7L23F70B following precipitation, which displays the saponin extract peaks, as well as a nitrate group peak around 1350 cm^{-1}, from nitrate detected in the precursors. Thereafter, FTIR for the prepared powders after the production treatment is shown in Fig. 4(c), with no visible changes in the peaks since the specimens were in solution form. Fig. 4(d) shows FTIR spectra for studied specimen after 2 h of calcination at 300 °C, which resulted in the elimination of saponin-related peaks and the emergence of M − O bond peaks between 400–600 cm^{-1}.

3.2. UV–VIS characterization

Fig. 5 shows the ultraviolet–visible (UV-VIS) spectra of all the samples. The highest absorbance of the 100B sample was approximately 285 nm, whereas the maximum absorbance of the other samples was blue-shifted. Fig. 6 shows Tauc's plots for the samples, which were created by plotting the photon energy hν versus $(\alpha h\nu)^2$, where α is the absorption coefficient of the material. Fig. 7 shows the bandgap values with respect to sample composition. The bandgap for pure bismuth oxide is shown to be approximately 3.16 eV, which is consistent with values of approximately 3.1 eV reported in the literature. In sample 30F70B, adding iron oxide to bismuth oxide decreased the bandgap to 3.13 eV, which is to be expected, as the bandgap of pristine iron oxide is approximately 2 eV. The band gap of lanthanum oxide is approximately 5.2 eV, and substituting lanthanum oxide in place of iron oxide in bismuth oxide increased the bandgap to 3.43, 3.45, 3.46, and 3.58 for samples 3L27F70B, 7L23F70B, 10L20F70B, and 20L10F70B, respectively (see Table 1).

3.3. Gamma ray shielding parameters

The mass attenuation coefficient μ/ρ is a commonly used parameter for classification of a material as either a good or bad absorber of photons. A higher mass attenuation coefficient is an indication that more photons interact and thus are absorbed by the interacting medium. μ/ρ values for the different samples of NP composites at different photon energy levels are shown in Table 2, and the energy and sample variation are shown in Fig. 8. The value of μ/ρ changes with the incident photon
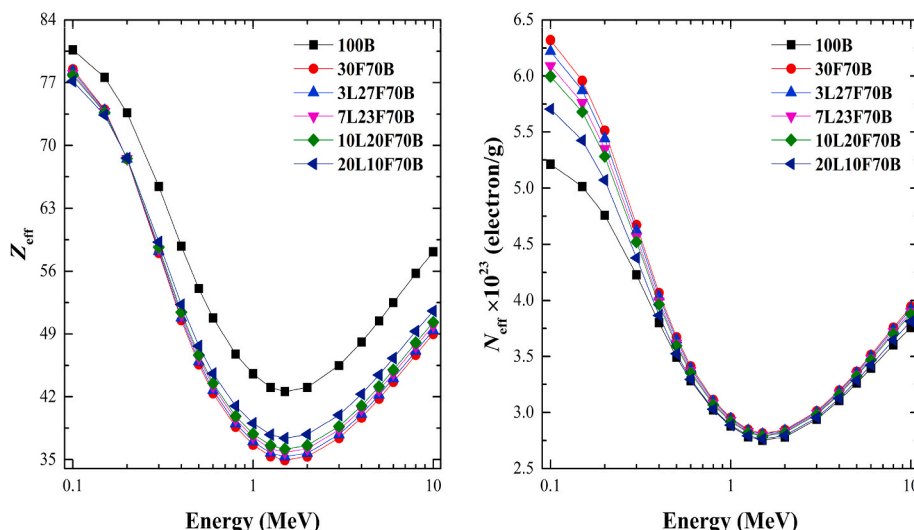

Fig. 9. Variations of effective atomic number (Z_{eff}) and effective electron density (N_{eff}) with respect to a function of photon energy in the prepared nanopowders.

Table 3
Mass energy-absorption coefficient of the prepared nanopowders via XCOM at different photon energies.

Energy (MeV)	μ_{en}/ρ (cm^2/g)					
	100B	30F70B	3L27F70B	7L23F70B	10L20F70B	20L10F70B
0.1	1.75245	1.54843	1.55983	1.57457	1.58530	1.61917
0.15	0.96326	0.84799	0.84840	0.84893	0.84931	0.85052
0.2	0.54221	0.47812	0.47739	0.47643	0.47574	0.47355
0.3	0.23008	0.20473	0.20412	0.20332	0.20274	0.20091
0.4	0.12988	0.11710	0.11670	0.11617	0.11579	0.11459
0.5	0.08748	0.08003	0.07975	0.07938	0.07912	0.07828
0.6	0.06599	0.06122	0.06101	0.06074	0.06054	0.05992
0.8	0.04565	0.04335	0.04321	0.04304	0.04291	0.04252
1	0.03634	0.03509	0.03499	0.03487	0.03477	0.03448
1.25	0.03001	0.02941	0.02933	0.02924	0.02917	0.02895
1.5	0.02665	0.02633	0.02627	0.02619	0.02614	0.02596
2	0.02385	0.02367	0.02362	0.02356	0.02352	0.02338
3	0.02318	0.02284	0.02281	0.02278	0.02275	0.02267
4	0.02414	0.02355	0.02354	0.02353	0.02352	0.02349
5	0.02536	0.02457	0.02457	0.02458	0.02458	0.02459
6	0.02658	0.02561	0.02562	0.02564	0.02565	0.02569
8	0.02869	0.02745	0.02748	0.02752	0.02755	0.02763
10	0.03035	0.02892	0.02896	0.02902	0.02906	0.02918

Table 4
Specific gamma ray constant of the prepared nanopowders via XCOM at different photon energies.

Energy (MeV)	$\Gamma (Rm^2/Cih)$					
	100B	30F70B	3L27F70B	7L23F70B	10L20F70B	20L10F70B
0.1	115.25542	101.83698	102.58686	103.55656	104.26219	106.48957
0.15	95.02735	83.65602	83.69620	83.74816	83.78597	83.90532
0.2	71.32010	62.89039	62.79351	62.66823	62.57706	62.28928
0.3	45.39602	40.39474	40.27311	40.11583	40.00139	39.64012
0.4	34.16682	30.80630	30.69975	30.56197	30.46171	30.14522
0.5	28.76567	26.31612	26.22358	26.10391	26.01683	25.74197
0.6	26.03932	24.15611	24.07354	23.96677	23.88908	23.64382
0.8	24.01989	22.80750	22.73691	22.64562	22.57920	22.36952
1	23.89735	23.07766	23.01335	22.93019	22.86968	22.67866
1.25	24.67029	24.17579	24.11537	24.03723	23.98037	23.80089
1.5	26.28995	25.97724	25.91772	25.84076	25.78476	25.60799
2	31.37111	31.13426	31.07369	30.99536	30.93836	30.75844
3	45.73614	45.05682	45.00542	44.93895	44.89059	44.73791
4	63.50335	61.96577	61.93827	61.90271	61.87684	61.79516
5	83.40976	80.79275	80.80260	80.81533	80.82460	80.85386
6	104.89776	101.05613	101.10888	101.17708	101.22671	101.38338
8	150.94467	144.42025	144.57814	144.78232	144.93089	145.39987
10	199.59230	190.20385	190.48173	190.84108	191.10256	191.92796

energy E and the NP composition. Values of μ/ρ in the ranges of 0.0412–5.1624, 0.0401–4.5406, 0.0401–4.5285, 0.0401–4.5129, 0.0401–4.5015, and 0.0400–4.4156 cm^2/g were obtained for 100B, 30F70B, 3L27F70B, 7L23F70B, 10L20F70B, and 20L10F70B, respectively. This shows that at a given photon energy, there was a gradual but small decrease in the value of μ/ρ as the molar concentration of Bi_2O_3 decreased in the nanocomposite. At 0.1 MeV, the replacement of 30 mol % of Bi_2O_3 by Fe_2O_3 resulted in a decrease of approximately 12.05% n the mass attenuation coefficient of 100B. A further replacement of 3 mol % of Fe_2O_3 by La_2O_3 NP led to a further 0.27% decrease in the μ/ρ value of 30F70B. A further increase in the molar concentration of La_2O_3 NP at the expense of Fe_2O_3 resulted in a marginal decrease in the value of the mass attenuation coefficient. This trend in μ/ρ (100B > 30F70B > 3L27F70B > 7L23F70B > 10L20F70B > 20L10F70B) was maintained throughout the 0.1–10 MeV energy spectrum, although it was more visible in the lower-energy region. This trend is attributable to the μ/ρ values of Bi_2O_3, Fe_2O_3, and La_2O_3. The relatively higher μ/ρ value for Bi_2O_3 relative to those of Fe_2O_3 and La_2O_3 clearly influences the attenuation coefficient of the nanocomposite. For example, at 0.1 MeV, the mass attenuation coefficient of Bi_2O_3 is 4.97 cm^2/g, compared to

0.27 and 1.90 cm^2/g for Fe_2O_3 and La_2O_3, respectively. As the proportion of Fe_2O_3, and La_2O_3 NP increases in the nanocomposite, the weight fraction and hence partial μ/ρ due to Bi_2O_3 decrease. This in turn reduces the total attenuation coefficient of the nanocomposite. Furthermore, for each composite, the mass attenuation coefficient decreases with the photon energy E within the range $0.1 \leq E \leq 4$ MeV, above which a gradual rise was observed as energy progresses. This behaviour of μ/ρ is similar to that observed for other materials [14–23] and consistent with theory [48]. Theoretically, the interactions leading to photon absorption, such as the photoelectric effect and Compton scattering, are significant at low energies, and they decrease with E. The other major interaction is the pair production process, which increases slowly as E increases. The minimum value of the attenuation coefficient obtained at 4 MeV indicates that the pair production process begins to be significant at this energy level. This transition energy depends strongly on the chemical composition of the interacting medium. The consistent minimum value of the mass attenuation coefficient for all of the composite samples could be attributed to the similar value of the number of electrons per unit mass in the materials.

In Fig. 9a and b, the variation in Z_{eff} and N_{eff} with respect to E is illustrated for 100B, 30F70B, 3L27F70B, 7L23F70B, 10L20F70B, and 20L10F70B. The effective atomic number can be seen as the effective
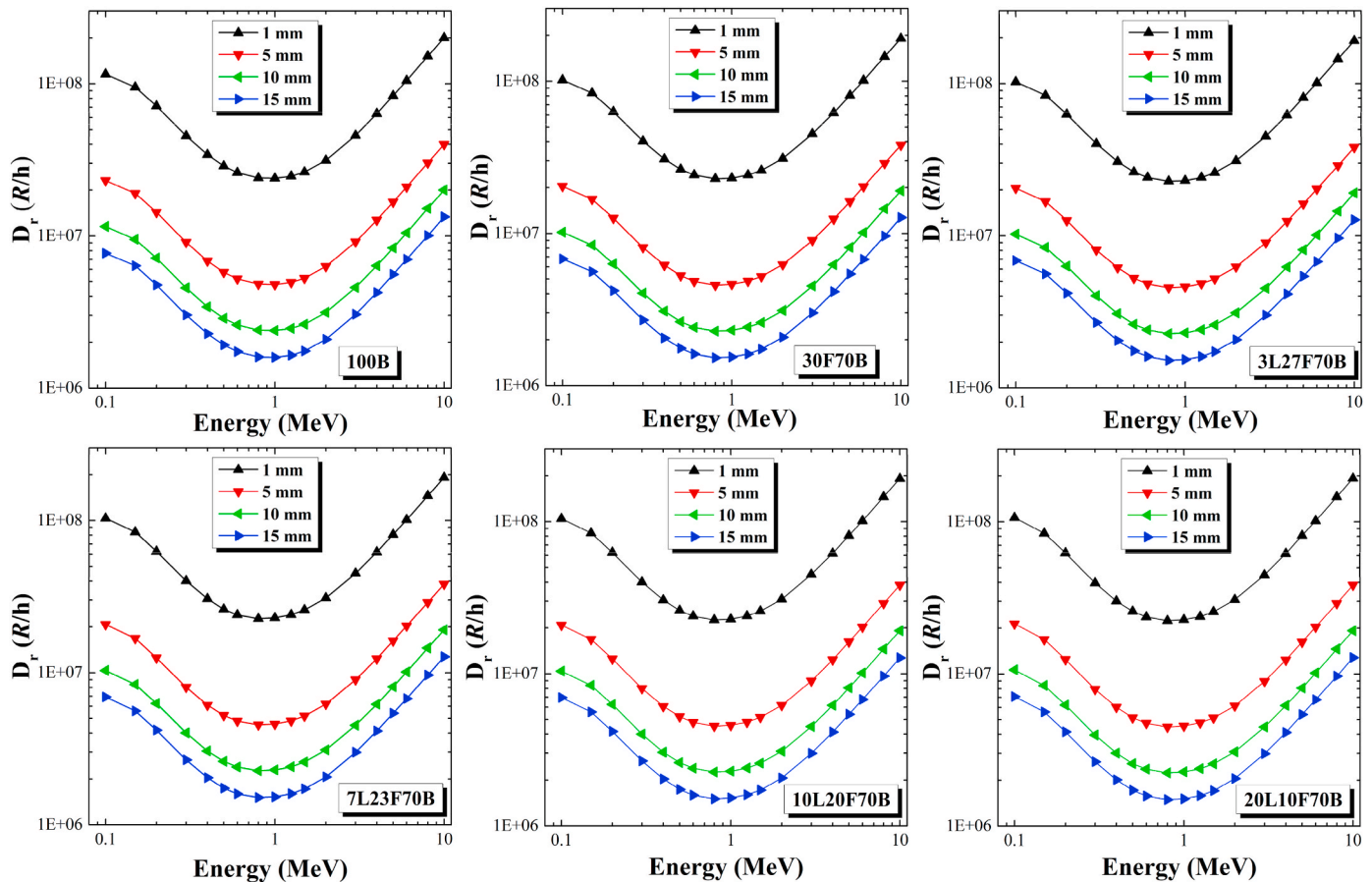
Fig. 10. Variation of gamma dose rate (D_r) at different energy levels for the prepared nanopowders.

atomic number of a compound or mixture, which is a parameter that is very important in radiation dosimetric and shielding calculation. In shielding, equal values of Z_{eff} indicate similar photon interaction/energy loss processes and hence comparable shielding effectiveness. Clearly, the behaviour of Z_{eff} with respect to E is similar to that of the mass attenuation coefficient, albeit with more conspicuous variation as the chemical composition of the composite changes. This shows that Z_{eff} is more sensitive to differences in the chemical makeup of a photon-interacting medium. The Z_{eff} dependence of the photoelectric effect, Compton scattering, and pair production explain the energy behaviour of Z_{eff}. Throughout the energy spectrum, 100B exhibited the highest Z_{eff} because Bi has a higher atomic number than La and Fe. The higher atomic number of La than of Fe is responsible for the trend 30F70B < L27F70B < 7L23F70B < 10L20F70B < 20L10F70B for the Z_{eff} of the remaining composites. N_{eff} is the number of available electrons per unit gram of the interacting substance. N_{eff} is directly proportional to the effective number and inversely proportional to the mass per mole of the nanocomposites, which explains the order 30F70B > L27F70B > 7L23F70B > 10L20F70B > 20L10F70B > 100B.

The mass energy absorption coefficient μ_{en}/ρ is a crucial quantity in determining the photon energy absorbed. For dosimetric material, the μ_{en}/ρ is an invaluable photon interaction quantity. The μ_{en}/ρ values of the nanocomposites at respective energy levels are presented in Table 3. The μ_{en}/ρ values clearly change with respect to E and the chemical speciation of the composites. Mass energy absorption coefficient changes in the ranges of 0.0232–1.7525, 0.0228–1.5484, 0.0228–1.5598, 0.0288–1.5746, 0.0228–1.5853, 0.0227–1.6192 cm^2/g were obtained for 100B, 30F70B, 3L27F70B, 7L23F70B, 10L20F70B, and 20L10F70B, respectively. The minimum μ_{en}/ρ was obtained at 3 MeV because of the

dominance of Compton scattering, which leads to lower energy absorption than the photoelectric effect and pair production. Furthermore, an increase in the La content of the glasses led to more photon energy absorption, as indicated by the following order of μ_{en}/ρ values: 100B > 20L10F70B > 10L20F70B > 7L23F70B > 3L27F70B > 30F70B. In addition, it is obvious that the energy dependence of μ_{en}/ρ is similar to that of μ/ρ, as shown in equation (6) [49]:

$$\mu_{en}/\rho = \frac{E_{en}}{E}\,\mu/\rho \tag{6}$$

where E and E_{en} are the incident and absorbed photon energy, respectively.

The specific gamma ray constant Γ of each of the prepared nanopowders is the absorbed dose at a distance of 1 m from a photon source. The values of Γ vary with E in a manner similar to that of μ_{en}/ρ, as suggested by equation (4). At a photon energy of 10 MeV, Γ is equal to 199.52, 190.20, 190.48.190.84, 191.84, 191.10, and 191.93 Rm^{2}Ci^{-1}h^{-1} for 100B, 30F70B, 3L27F70B, 7L23F70B, 10L20F70B, and 20L10F70B, respectively as can be seen in Table 4. The calculated absorbed dose rate $\dot{D}$ for the prepared nanopowders is shown in Fig. 10. The influences of μ_{en}/ρ, Γ, and thickness on $\dot{D}$ are obvious. Based on the analysed photon interaction parameters, it is clear that 100B is the best photon absorber among the investigated nanoparticles. Among the nanocomposites containing Bi$_2$O$_3$, Fe$_2$O$_3$, and La$_2$O$_3$ nanoparticles, 20L10F70B exhibited the best photon energy absorption.

4. Conclusion

Nanopowders with chemical representations of $100Bi_2O_3$ (100B), $30Fe_2O_3–70Bi_2O_3$ (30F70B), $3La_2O_3–27Fe_2O_3–70Bi_2O_3$ (3L27F70B), $7La_2O_3–23Fe_2O_3–70Bi_2O_3$ (7L23F70B), $10La_2O_3–20Fe_2O_3–70Bi_2O_3$ (10L20F70B), and $20La_2O_3–10Fe_2O_3–70Bi_2O_3$ (20L10F70B) were successfully synthesized by the microwave-assisted hydrothermal method. Saponin extract from soapnuts was used as the nanoparticle capping agent. The structural, optical, and gamma radiation characteristics were measured, calculated, and analysed, respectively. The result of the analysis suggest that the chemical structures of the nanocomposites influenced their optical and radiation-shielding characteristics. Adding Fe_2O_3 decreased the optical band gap of 100B, while the addition of La_2O_3 increased that of 30F70B. The ranges of mass attenuation coefficients of the nanocomposites computed via XCOM were 0.0412–5.1624, 0.0401–4.5406, 0.0401–4.5285, 0.0401–4.5129, 0.0401–4.5015, and 0.0400–4.4156 cm^2/g for 100B, 30F70B, 3L27F70B, 7L23F70B, 10L20F70B, and 20L10F70B, respectively. The ranges of mass energy absorption coefficients were 0.0232–1.7525, 0.0228–1.5484, 0.0228–1.5598, 0.0288–1.5746, 0.0228–1.5853, and 0.0227–1.6192 cm^2/g, respectively for a photon energy range of 0.1–10 MeV. The results of the analysis of the photon interaction parameters show that the synthesized nanopowders could function well as fillers in radiation-shielding matrices.

Declaration of competing interest

The authors declare that they have no known competing financial interests or personal relationships that could have appeared to influence the work reported in this paper.

Acknowledgement

References

[1] Can Zhang, Bei Xie, Yujian Zou, Dan Zhu, Lei Lei, Dapeng Zhao, Hemin Nie, Zero-dimensional, one-dimensional, two-dimensional and three-dimensional biomaterials for cell fate regulation, Adv. Drug Deliv. Rev. 132 (2018) 33–56.

[2] Ibrahim Khan, Khalid Saeed, Idrees Khan, Nanoparticles: properties, applications and toxicities, Arab. J. Chem. 12 (7) (2019) 908–931.

[3] Augustine D. Terna, E. Elias, Justina I. Elemike, Omosede E. Mbonu, Osafile, Rachael O. Ezeani, The future of semiconductors nanoparticles: synthesis, properties and applications, Mater. Sci. Eng., B 272 (2021), 115363.

[4] Hassanein, Farghaly Taha, Aya Samir Mohammed, Wael Mohamed, Rokaya Aly Sobh, Magdy Kandil Zahran, Optimized synthesis of biopolymer-based zinc oxide Nanoparticles and evaluation of their antibacterial activity, Egypt. J. Chem. 64 (7) (2021) 3767–3790.

[5] Yen Pin Yew, Kamyar Shameli, Mikio Miyake, Nurul Bahiyah Bt, Ahmad Khairudin, Shaza Eva Bt Mohamad, Takeru Naiki, Kar Xin Lee, Green biosynthesis of superparamagnetic magnetite Fe3O4 nanoparticles and biomedical applications in targeted anticancer drug delivery system: a review, Arab. J. Chem. 13 (1) (2020) 2287–2308.

[6] Aini Norhidayah Mohamed, Nuruljannah Janurin, Yasmin Amirah Che Yahaya, Surface-active properties of extracted saponin from the leaves of nephelium lappaceum, Curr. Sci. Technol. 1 (1) (2021) 44–49.

[7] A.R. Mainkar, C.I. Jolly, Evaluation of commercial herbal shampoos, Int. J. Cosmet. Sci. 22 (5) (2000) 385–391.

[8] Abhirup Basu, Soham Basu, Sujaya Bandyopadhyay, Ranjana Chowdhury, Optimization of evaporative extraction of natural emulsifier cum surfactant from Sapindus mukorossi—characterization and cost analysis, Ind. Crop. Prod. 77 (2015) 920–931.

[9] A.B. Chhetri, K.C. Watts, M.S. Rahman, M.R. Islam, Soapnut extract as a natural surfactant for enhanced oil recovery, Energy Sources, Part A Recovery, Util. Environ. Eff. 31 (20) (2009) 1893–1903.

[10] Ebrahim Najafi, Kwanwoo Shin, Radiation resistant polymer–carbon nanotube nanocomposite thin films, Colloids Surf. A Physicochem. Eng. Asp. 257 (2005) 333–337.

[11] N. Hashimoto, S. Oie, H. Homma, S. Ohnuki, In-situ observations of microstructure evolution in electron-irradiated multi-wall carbon nanotubes, Mater. Trans. 55 (3) (2014) 458–460.

[12] Zhenhao Li, Siyuan Chen, Shruti Nambiar, Yonghai Sun, Mingyu Zhang, Wanping Zheng, John TW. Yeow, PMMA/MWCNT nanocomposite for proton radiation shielding applications, Nanotechnology 27 (23) (2016), 234001.

[13] M. Rashad, H.O. Tekin, M.H. Hesham, Zakaly, Mariia Pyshkina, AM Issa Shams, G. Susoy, Physical and nuclear shielding properties of newly synthesized magnesium oxide and zinc oxide nanoparticles, Nucl. Eng. Technol. 52 (9) (2020) 2078–2084.

[14] Asghar Mesbahi, Hosein Ghiasi, Shielding properties of the ordinary concrete loaded with micro-and nano-particles against neutron and gamma radiations, Appl. Radiat. Isot. 136 (2018) 27–31.

[15] Huseyin Ozan Tekin, Viswanath P. Singh, Tugba Manici, Effects of micro-sized and nano-sized WO3 on mass attenuation coefficients of concrete by using MCNPX code, Appl. Radiat. Isot. 121 (2017) 122–125.

[16] Khatibeh Verdipoor, Abdolali Alemi, Asghar Mesbahi, Photon mass attenuation coefficients of a silicon resin loaded with WO3, PbO, and Bi2O3 Micro and Nano-particles for radiation shielding, Radiat. Phys. Chem. 147 (2018) 85–90.

[17] B. AlsharIani, I.O. Olarinoye, C. Mutuwong, Chahkrit Sriwunkum, H.A. Yakout, H. O. Tekin, M.S. Al-Buriahi, Amorphous alloys with high Fe content for radiation shielding applications, Radiat. Phys. Chem. 183 (2021), 109386.

[18] M.S. Al-Buriahi, Z.A. Alrowaili, Canel Eke, Jamila S. Alzahrani, I.O. Olarinoye, Sriwunkum Chahkrit, Optical and radiation shielding studies on tellurite glass system containing ZnO and Na2O, Optik 257 (2022) 168821.

[19] Nada Alfryyan, Z.A. Alrowaili, H.H. Somaily, I.O. Olarinoye, Norah Alwadai, C. Mutuwong, M.S. Al-Buriahi, Comparison of radiation shielding and elastic properties of germinate tellurite glasses with the addition of Ga2O3, J. Taibah. Univ. Soc. 16 (1) (2022) 183–192.

[20] Imen Kebaili, S. Znaidia, Jamila S. Alzahrani, Miysoon A. Alothman, Imed Boukhris, I.O. Olarinoye, C. Mutuwong, M.S. Al-Buriahi, Ge 20 Se 80-x Bi x (x≤ 12) chalcogenide glasses for infrared and gamma sensing applications: structural, optical and gamma attenuation aspects, J. Mater. Sci. Mater. Electron. (2021) 1–14.

[21] Taranjot Kaur, Yogesh K. Vermani, M.S. Al-Buriahi, Jamila Alzahrani, Tejbir Singh, Comprehensive investigations on radiation shielding efficacy of bulk and nano Pb-Sn-Cd-Zn alloys, Phys. Scripta (2022).

[22] S.A. Abo-El-Enein, F.I. El-Hosiny, S.M.A. El-Gamal, M.S. Amin, dan M. Ramadan, Gamma radiation shielding, fire resistance and physicochemical characteristics of Portland cement pastes modified with synthesized Fe2O3 and ZnO nanoparticles, Construct. Build. Mater. 173 (2018) 687–706.

[23] M.S. Al-Buriahi, I.O. Olarinoye, B. Alsharani, Ateyyah M. Al-Baradi, Chalermpon Mutuwong, Halil Arslan, Optical and gamma-ray absorption features of newly developed P2O5– Ce2O3– La2O3 glass system, Appl. Phys. A 127 (11) (2021) 1–9.

[24] Siyuan Chen, Shruti Nambiar, Zhenhao Li, Ernest Osei, Darko Johnson, Wanping Zheng, Zhendong Sun, Ping Liu, John TW. Yeow, Bismuth oxide-based nanocomposite for high-energy electron radiation shielding, J. Mater. Sci. 54 (4) (2019) 3023–3034.

[25] Huda Ahmed Maghrabi, Arun Vijayan, Pradip Deb, Lijing Wang, Bismuth oxide-coated fabrics for X-ray shielding, Textil. Res. J. 86 (6) (2016) 649–658.

[26] S.A. Abo-El-Enein, F.I. El-Hosiny, S.M.A. El-Gamal, M.S. Amin, dan M. Ramadan, Gamma radiation shielding, fire resistance and physicochemical characteristics of Portland cement pastes modified with synthesized Fe2O3 and ZnO nanoparticles, Construct. Build. Mater. 173 (2018) 687–706.

[27] R. Irmawati, MN Noorfarizan Nasriah, Y.H. Taufiq-Yap, S.B. Abdul Hamid, Characterization of bismuth oxide catalysts prepared from bismuth trinitrate pentahydrate: influence of bismuth concentration, Catal. Today 93 (2004) 701–709.

[28] Jamila S. Alzahrani, Canel Eke, Z.A. Alrowaili, H.H. Somaily, Chahkrit Sriwunkum, M.S. Al-Buriahi, Evaluation of the radiation shielding characteristics of WO3–MoO3–TeO2/Sb2O3 glasses, Can. Metall. Q (2022) 1–11.

[29] Gharam A. Alharshan, Z.A. Alrowaili, Zakaria MM. Mahmoud, I.O. Olarinoye, M. S. Al-Buriahi, Effect of Nb2O5 inclusion on the radiation shielding efficiency of TeO2–ZnO–LiF–NaF glass system, Radiat. Phys. Chem. (2022), 110127.

[30] Avula Edukondalu, Salavadi Stalin, M. Srinivasa Reddy, Canel Eke, Z.A. Alrowaili, M.S. Al-Buriahi, Synthesis, thermal, optical, mechanical and radiation-attenuation characteristics of borate glass system modified by Bi2O3/MgO, Appl. Phys. A 128 (4) (2022) 1–12.

[31] Jamila S. Alzahrani, Andrei V. Lebedev, Samvel A. Avanesov, Alaa Hammoud, Z. A. Alrowaili, Zakaria Mm Mahmoud, I.O. Olarinoye, M.S. Al-Buriahi, Synthesis and properties of tellurite based glasses containing Na2O, BaO, and TiO2: Raman, UV and neutron/charged particle shielding assessments, Ceram. Int. (2022).

[32] Z.Y. Khattari, M.S. Al-Buriahi, Monte Carlo simulations and Phy-X/PSD study of radiation shielding effectiveness and elastic properties of barium zinc aluminoborosilicate glasses, Radiat. Phys. Chem. (2022), 110091.

[33] Jamila S. Alzahrani, Z.A. Alrowaili, Canel Eke, Zakaria MM. Mahmoud, C. Mutuwong, M.S. Al-Buriahi, Nuclear shielding properties of Ni-, Fe-, Pb-, and W-based alloys, Radiat. Phys. Chem. (2022), 110090.

[34] M.S. Al-Buriahi, Z.A. Alrowaili, Sultan Alomairy, I.O. Olarinoye, Mutuwong Chalermpon, Optical properties and radiation shielding competence of Bi/Te-BGe glass system containing B2O3 and GeO2, Optik 257 (2022), 168883.

[35] B. Srinivas, Ashok Bhogi, Pallati Naresh, M. Narasimha Chary, Md Shareefuddin, Z. A. Alrowaili, Zakaria MM. Mahmoud, I.O. Olarinoye, M.S. Al-Buriahi, Fabrication, optical and radiation shielding properties of BaO-TeO2-B2O3-Cr2O3 glass system, Optik 258 (2022) 168877.

[36] Jamila S. Alzahrani, Amandeep Sharma, S.N. Nazrin, Z.A. Alrowaili, M.S. Al-Buriahi, Optical and radiation shielding effectiveness of a newly fabricated WO3 doped TeO2–B2O3 glass system, Radiat. Phys. Chem. (2022), 109968.

[37] Miysoon A. Alothman, I.O. Olarinoye, Chahkrit Sriwunkum, Sultan Alomairy, Jamila S. Alzahrani, M.S. Al-Buriahi, Study of the radiation attenuation properties of MgO-Al2O3-SiO2-Li2O-Na2O glass system, J. Australas. Ceram. Soc. 58 (1) (2022) 267–273.

[38] Karthikeyan, S., and M. Selvapandiyan. "IINTERNATIONAL JOURNAL OF ENGINEERING SCIENCES & RESEARCH TECHNOLOGY EFFECT OF ANNEALING TEMPERATURE ON THE PROPERTIES OF LANTHANUM OXIDE (LA2O3) NANOPLATES BY REFLUX ROUTES.".

[39] Yayuk Astuti, Arnelli Arnelli, Pardoyo Pardoyo, Amilia Fauziyah, Siti Nurhayati, Arum Dista Wulansari, Rizka Andianingrum, Hendri Widiyandari, Gaurav A. Bhaduri, Studying impact of different precipitating agents on crystal structure, morphology and photocatalytic activity of bismuth oxide, Bull. Chem. React. Eng. Catal. 12 (3) (2017) 478–484.

[40] Xiaodie Zhu, Ziyang Lu, Xinlin Liu, Minshan Song, Guosheng Zhou, Zehui Yu, Lingyan Xu, Qian Liu, Song Han, Jinyu Chu, Continuous microwave synthesis of Bi 2 O 3 rods coated with a temperature-sensitive polymer, J. Mater. Sci. 55 (2020) 11213–11225.

[41] Nurudeen Yekeen, Azlinda Abdul Malik, Kamal Ahmad, Idris Nadia Izwani Reepei, Ganie Kenny, Foaming properties, wettability alteration and interfacial tension reduction by saponin extracted from soapnut (Sapindus Mukorossi) at room and reservoir conditions, J. Petrol. Sci. Eng. 195 (2020), 107591.

[42] Babli Debnath, Ratan Das, Controlled synthesis of saponin-capped silver nanotriangles and their optical properties, Plasmonics 14 (6) (2019) 1365–1375.

[43] I. Nowrouzi, A.H. Mohammadi, A.K. Manshad, Water-oil interfacial tension (IFT) reduction and wettability alteration in surfactant flooding process using extracted saponin from Anabasis Setifera plant, J. Petrol. Sci. Eng. 189 (2020), 106901.

[44] Zhenbao Zhu, Ying Wen, Jianhua Yi, Yungang Cao, Fuguo Liu, David Julian McClements, Comparison of natural and synthetic surfactants at forming and stabilizing nanoemulsions: tea saponin, Quillaja saponin, and Tween 80, J. Colloid Interface Sci. 536 (2019) 80–87.

[45] Kulbhushan Samal, Chandan Das, Kaustubha Mohanty, Eco-friendly biosurfactant saponin for the solubilization of cationic and anionic dyes in aqueous system, Dyes Pigments 140 (2017) 100–108.

[46] Monohar Hossain Mondal, Susanta Malik, Garain Amit, Sangita Mandal, Bidyut Saha, Extraction of natural surfactant saponin from soapnut (Sapindus mukorossi) and its utilization in the remediation of hexavalent chromium from contaminated water, Tenside Surfactants Deterg. 54 (6) (2017) 519–529.

[47] Almutairi, Meshari Saad, Muhammad Ali, Direct detection of saponins in crude extracts of soapnuts by FTIR, Nat. Prod. Res. 29 (13) (2015) 1271–1275.

[48] Attix, Frank Herbert, Introduction to Radiological Physics and Radiation Dosimetry, John Wiley & Sons, 2008.

[49] Baris T. Tonguc, Halil Arslan, Sultan Mohammed, Al-Buriahi, Studies on mass attenuation coefficients, effective atomic numbers and electron densities for some biomolecules, Radiat. Phys. Chem. 153 (2018) 86–91.